Microporous and Mesoporous Materials 331 (2022) 111641

Contents lists available at ScienceDirect

Microporous and Mesoporous Materials

journal homepage: www.elsevier.com/locate/micromeso

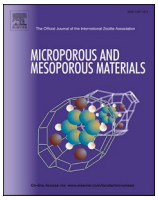

Mesoporous silicon nanoparticles covered with PEG molecules by mechanical grinding in aqueous suspensions

A.S. Eremina [a,*], Yu. V. Kargina [a,b], A. Yu. Kharin [a], D.I. Petukhov [c], V. Yu. Timoshenko [a,b,d,**]

[a] National Research Nuclear University «MEPhI», Moscow, Russia
[b] Lomonosov Moscow State University, Faculty of Physics, Moscow, Russia
[c] Lomonosov Moscow State University, Faculty of Chemistry, Moscow, Russia
[d] Lebedev Physical Institute of the Russian Academy of Sciences, Moscow, Russia

ARTICLE INFO

Keywords:
Mesoporous silicon
Nanoparticles
Polyethylene glycol
PEGylation
Surface coating
Infrared spectroscopy

ABSTRACT

We propose a one-step procedure to stabilize mesoporous silicon nanoparticles in aqueous solutions by polyethylene glycol (PEG) coating during grinding in a planetary ball mill. The milling is done in aqueous medium that allows us to directly obtain the aqueous suspension of PEGylated nanoparticles. The prepared nanoparticles are investigated by means of the scanning electron microscopy, energy dispersive X-ray spectroscopy, low-temperature nitrogen sorption, dynamic light scattering, Fourier transform infrared spectroscopy, Raman and photoluminescence spectroscopy, which reveal the nanoparticle size of 50–100 nm, preservation of the nanocrystallinity and mesopores. The PEGylated nanoparticles are found to be stable in aqueous solution for at least 24 h. The proposed PEGylation method can be used to control the physical properties and stability of mesoporous silicon nanoparticles for biomedical applications.

1. Introduction

Mesoporous silicon (mPSi) is a promising material for biomedical applications because of its low toxicity, biodegradability, and ability to act as an active agent for various therapeutic procedures [1]. Nanoparticles (NPs) of mPSi are widely explored as nanocontainers of anticancer drugs [2–4] as well as they exhibit properties of sensitizers for mild methods of cancer therapy [1,5]. When NPs are prepared by high energy mechanical grinding of electrochemically grown mPSi films, they represent typically 100 nm aggregates of small (2–5 nm) silicon (Si) nanocrystallites [5]. It was found that both mPSi and crystalline Si (c-Si) NPs can dissolve in water and aqueous solutions [3,6,7]. The dissolution rate of c-Si wafers in water is known to be determined by the orientation of c-Si surface and the pH level of the solution [8]. While the pH-depended dissolution of mPSi and Si-NPs was also observed in different studies (see, for example, Refs. [9,10]), the dissolution rate depended on the morphology, size, and surface coating of NPs [7,11].

To prevent the rapid dissolution of mPSi-NPs and to stabilize their properties in aqueous medium the NP' surface should be coated by desired molecules [2,12]. The surface coating can be realized by using physical adsorption of biopolymer molecules [13]. It was found that dextran-coated mPSi-NPs were more stable against dissolution in water and exhibited higher efficiency as a sonosensitizer in sonodynamic therapy in comparison with uncoated mPSi-NPs [14].

Polyethylene glycol (PEG) is an inert hydrophilic polymer invisible to the immunological response, and the former is commonly used for surface coating of NPs, namely PEGylation [15–20]. *In vivo* tests of PEG with molecular weight up to 20 kDa facilitate by its ability to be excreted through urine [16]. Nevertheless, PEGylation of NPs usually requires nonpolar organic solvents or the creation of micelles to perform the coating with further solvent replacement. Such difficulties are caused by fast oxidation of the surface of Si-NPs in water, while an effective PEGylation requires the presence of hydrophobic Si–H bonds [15–20].

Our paper is aimed to develop an alternative method for the PEGylation of mPSi-NPs to reduce the dissolution rate of NPs and their stability in aqueous solution. The proposed one-step approach is based on mechanical grinding of mPSi films in aqueous solution of PEG, and it allows us to prepare directly aqueous suspensions of PEGylated mPSi-NPs.

* Corresponding author.
** Corresponding author. Lomonosov Moscow State University, Faculty of Physics, Moscow, Russia.
E-mail addresses: aseremina@mephi.ru (A.S. Eremina), timoshen@physics.msu.ru (V.Yu. Timoshenko).

https://doi.org/10.1016/j.micromeso.2021.111641
Received 5 October 2021; Received in revised form 2 December 2021; Accepted 14 December 2021
Available online 18 December 2021
1387-1811/

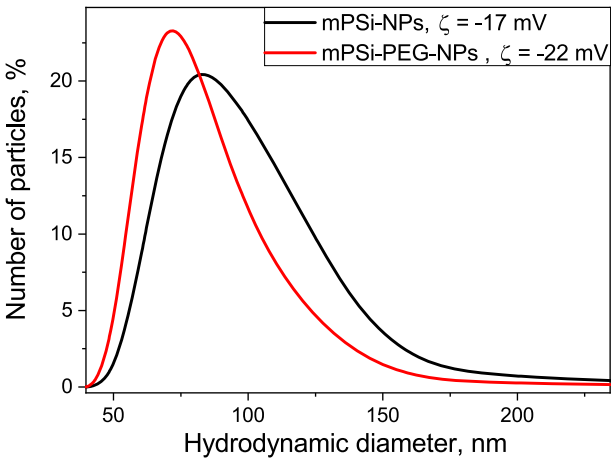

Fig. 1. Size distributions for mPSi-NPs (black curve) and mPSi-PEG-NPs (red curve) in aqueous solutions. The size (hydrodynamic diameter) and ZP (ζ) were measured by DLS. (For interpretation of the references to colour in this figure legend, the reader is referred to the Web version of this article.)

2. Materials and methods

First, mPSi films were formed by electrochemical etching (anodization) of boron-doped c-Si wafers with a resistivity of 20 mΩ cm in HF (48%):C_2H_5OH solution (1:1) at a current density of 50 mA/cm^2 and etching time of 1 h. The prepared films were separated from the substrate by applying a short (1–2 s) pulse of current with the current density of 500 mA/cm^2. Dried mPSi films were ground in a mortar to obtain powders.

Aqueous suspensions of mPSi-NPs were prepared by high-energy milling of mPSi powders in water or in 30% solution of PEG-400 (molecular mass of 400 Da) using a FRITSCH planetary ball mill Pulverisette 7 premium line (ZrO_2 milling balls with diameter of 3 mm, milling time 30 min amd rotation speed from 600 to 800 rpm) [9]. The prepared suspensions of mPSi-PEG-NPs were centrifuged to separate non-conjugated PEG in an Eppendorf Centrifuge 5804 for 30 min at 15000 rpm (21000 rcf). Resuspended samples were kept in distilled water in dialysis bags (pore sizes of 6–8 kDa) at room temperature with constant stirring. Aliquots of suspensions were analyzed after 3, 6 and 24 h of the dialysis.

To study the porosity and pore size distributions for mPSi-NPs and mPSi-PEG-NPs the corresponding aqueous suspensions were dried at 60°C for 12 h in air and then the obtained powers were investigated by means of the low-temperature nitrogen sorption analysis with a NOVA 4200e gas sorption analyzer (Quantachrome Instruments, USA). Prior the sorption experiment, 50 mg powders of mPSi-NPs and mPSi-PEG-NPs were additionally subjected to the standard degassing in vacuum at 150°C for 24 h.

The colloidal stability of mPSi-NPs and mPSi-PEG-NPs in aqueous medium was analyzed by using a method of the dynamic light scattering (DLS) with a Zetasizer Nano ZS apparatus (Malvern, UK), which was also used for zetta-potential (ZP) measurements. The DLS data were processed using the Zetasizer Software. The structural properties and composition of the dried NPs were investigated by means of the scanning electron microscopy (SEM) with a Tescan MAIA 3 SEM (Tescan, Czech Republic) equipped with an Inca X-act energy dispersive X-ray (EDX) spectroscopy analyzer.

Chemical bonds in the prepared samples were studied by using a Bruker IFS-66v/S Fourier-transform infrared (FTIR) spectrometer in the spectral range of 350–7500 cm^{-1} with resolution of 4 cm^{-1}. The prepared dried samples of mPSi and mPSi-PEG NPs were mixed with KBr to make tablets and tested for gradual release of PEG and silicon retention. The spectrum of PEG solution in water was also recorded by using a method of the attenuated total reflectance (ATR) with a ZnSe ATR-prism. Also, the nanocrystalline Si phase in the dried samples was probed by using a confocal Raman microscope Confotec MR350 (SOL instruments, Belarus) equipped with a semiconductor laser at a wavelength of 633 nm. The diameter of the laser spot was about 10 μm, and special attention was paid to reducing the excitation intensity to prevent photoheating of the studied samples.

3. Results and discussion

3.1. Dynamic light scattering

The binding of PEG to the surface of mPSi-NPs dispersed in water was probed by using the DLS method. Fig. 1 shows that the hydrodynamic diameter of NPs decreases and ZP becomes more negative for mPSi-PEG-NPs in comparison with that for mPSi-NPs. The observed change of the size distribution indicates a decrease of the agglomeration probability of mPSi-PEG-NPs where PEG molecules act as a surfactant. In other words, PEG molecules create a hydrophilic surface coating of mPSi-NPs that makes those NPs more negatively charged and it prevents the agglomeration of NPs in aqueous medium.

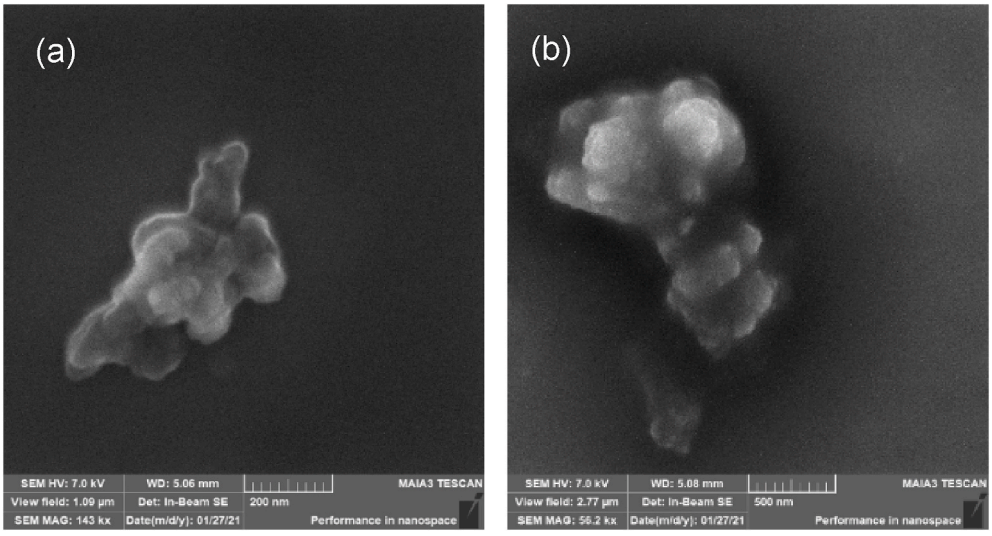

Fig. 2. SEM images: (a) mPSi-NPs and (b) mPSi-PEG-NPs.

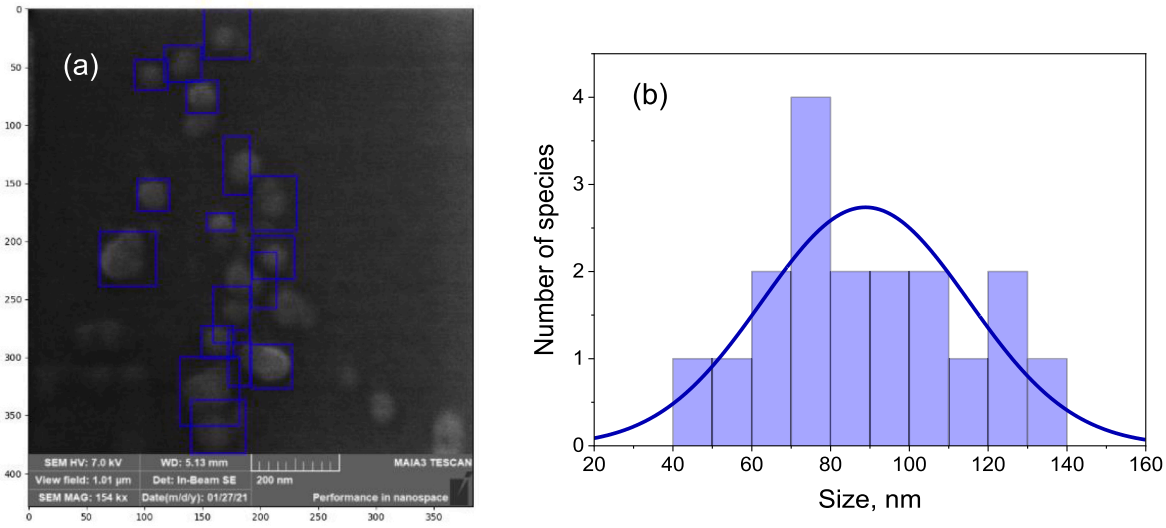

Fig. 3. (a) Typical SEM image with marked individual mPSi-NPs for the neural network analysis [21] and (b) histogram of the size distribution for mPSi-NPs.

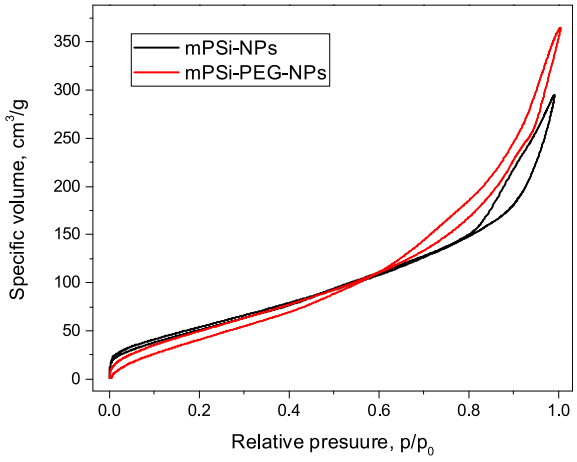

Fig. 4. Isotherms of adsorption and desorption of molecular nitrogen for mPSi-NPs (black curve) and mPSi-PEG-NPs (red curve). (For interpretation of the references to colour in this figure legend, the reader is referred to the Web version of this article.)

3.2. Scanning electron microscopy

Fig. 2 shows SEM images of mPSi-NPs and those after PEGylation. The size distribution of NPs obtained by using a neural network analysis [21] is characterized by an average particle size of 80 ± 25 nm (see Fig. 3). The average NP' size and morphology do not change significantly after PEGylation. The molecular weight of PEG-400 corresponds to the relatively small chain length and, therefore, the physical size of NPs hardly changes (compare Fig. 2a and b). At the same time, the PEGylation of mPSi-NPs results in the decrease of their sizes according to the DLS data (see Fig. 1).

3.3. Porosity analysis

Fig. 4 shows typical nitrogen sorption isotherms for the dried powders of mPSi-NPs and mPSi-PEG-NPs. The isotherm shape is inherent for mesoporous Si formed by electrochemical etching of heavily doped p-type Si wafers [22]. The capillary condensation of nitrogen molecules takes place in the mesopores that results in the characteristic hysteresis loop. The molecule condensation in mPSi-PEG-NPs begins at lower pressures, that is explaned broader pore size distribution and presence of

Table 1
Porosity parameters of mPSi-NPs and mPSi-PEG-NPs form the BJH method.

Sample	Surface area by BET, m^2/g	Pore volume, %
mPSi-NPs	220	57
mPSi-PEG-NPs	224	60

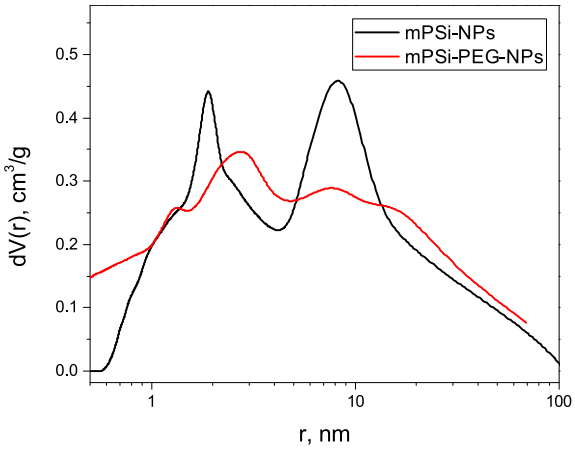

Fig. 5. Pore size distribution of mPSi-NPs (black curve) and mPSi-PEG-NPs (red curve) according to the BJH method. (For interpretation of the references to colour in this figure legend, the reader is referred to the Web version of this article.)

smaller pores. The specific surface area estimated by using the BET method is about 220 and 224 m^2/g for mPSi-NPs and mPSi-PEG-NPs, respectively (see Table 1).

The BJH method was used to determine the pore size distribution and porosity (volume of pores) for mPSi-NPs and mPSi-PEG-NPs. As one can see from Fig. 5 the pore size distribution in mPSi-NPs (black curve in Fig. 5) consists of two main types of pores, i.e. small (with radius $r < 2–3$ nm) pores and larger ($r > 5$ nm) ones. The larger pores are probably formed during mechanical grinding of mPSi layers in water followed by drying in air [23]. The pore size distribution for mPSi-PEG-NPs exhibit the main broad peak with a maximum at about 3 nm with low-size and large-size shoulders at $r < 1.5$ nm and $r > 5$ nm, respectively. While the low-size shoulder can be related to micropores formed during the drying of PEG coatings of mPSi-PEG-NPs, the main peak and large-size

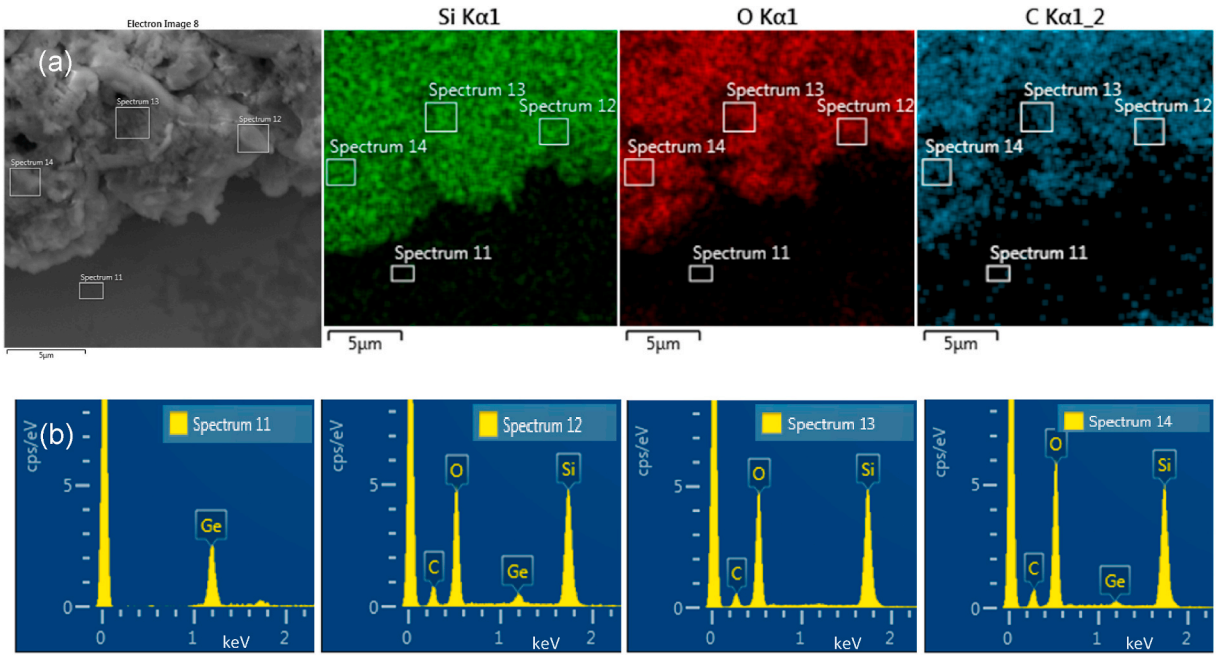

Fig. 6. EDX analysis of mPSi-PEG-NPs: (a) distribution map of elements and (b) EDX spectra in different points.

Table 2
Content of the main chemical elements in mPSi-PEG-NPs estimated from the corresponding EDX spectra with subtracted c-Ge background.

Element	Line Type	Weight %	Atomic %
Si	K series	46	31
O	K series	44	53
C	K series	10	16
Total		100.00	100.00

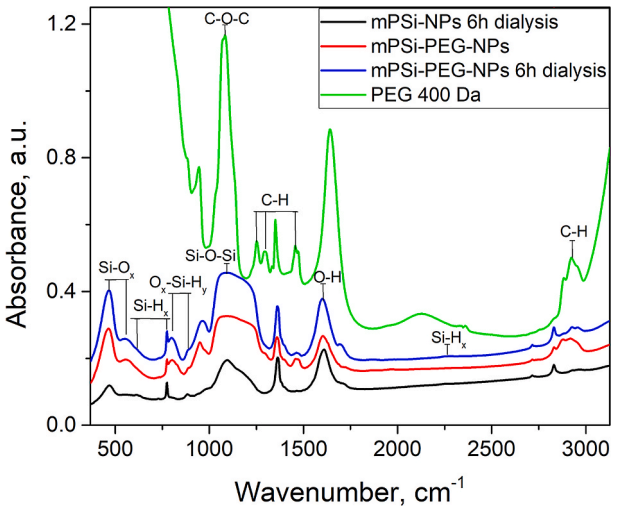

Fig. 7. FTIR absorption spectra of mPSi-NPs after 6 h dialysis (black curve), mPSi-PEG-NPs (red curve), mPSi-PEG-NPs after 6 h dialysis (blue curve), and PEG 400 Da (green curve); 30 scans, 4 cm^{-1} spectral resolution. (For interpretation of the references to colour in this figure legend, the reader is referred to the Web version of this article.)

shoulders in the size distribution are probably related to the mesopores in mPSi-NPs and in agglomerates of those NPs, respectively. The porosity of mPSi-NPs and mPSi-PEG-NPs accounts 57 and 60% (see Table 1) that indicates the preservation of porous structure of mPSi-NPs after the used PEGylation procedure.

3.4. EDX spectroscopy

Fig. 6 (a) shows a SEM image and maps of the main chemical elements for mPSi-PEG-NPs deposited on crystalline germanium (c-Ge) substrate. The carbon mapping clearly indicates the presence of PEG on the surface of mPSi-PEG-NPs. Detailed values of the atomic and weight parts for three main elements, i.e. silicon (Si), oxygen (O) and carbon (C), in the investigated sample are given in Table 2.

According to the EDX data (see Table 2), mPSi-PEG-NPs consist of silicon (31 at.%), oxygen (53 at.%) and carbon (10 at.%). Note, the chemical composition of mPSi-NPs comprises only silicon and oxygen with concentration of about 45 and 55 at.% (see Fig. S1 and Tabl.S1 in Supplementary Materials). Despite the EDX spectroscopy is suitable for only approximate evaluations of the chemical composition of materials, the obtained EDX data indicate unambiguously both the presence of organic molecules of PEG-400 and an increase of the silicon oxide phase in mPSi-PEG-NPs in comparison with initial mPSi-NPs. More detail information about the chemical composition of the prepared samples is obtained from their FTIR spectra discussed below.

3.5. FTIR spectroscopy

Fig. 7 shows FTIR absorption spectra of mPSi-NPs and mPSi-PEG-NPs after 6 h of dialysis as well the FTIR spectra of PEG and as-prepared mPSi-PEG-NPs.

The FTIR spectrum of mPSi-NPs (black curve in Fig. 7) consists of intense absorption bands at 467 and 553 cm^{-1} related to the different vibration modes in SiO_x (x = 1.5–2) and intense absorption band at 1095 cm^{-1} (Si–O–Si) [1]. The spectrum shows also weaker absorption bands at 613 cm^{-1} (bending region) [1,24], 775 cm^{-1} (bending region) [25] and 2250 cm^{-1} (stretching vibrations) [24,25] related to the surface Si–H_x (x = 1,2,3) bonds as well a band at 810 and 890 cm^{-1} attributed to the O_x-Si-H_y (y = 1–3) bonds [1]. The appearance of the Si–O–Si and O_x-Si-H_y groups is obviously related to the oxidation of the samples in air.

The huge internal specific surface of as-prepared porous silicon is known to be covered by the Si-H_x bonds. According to the established

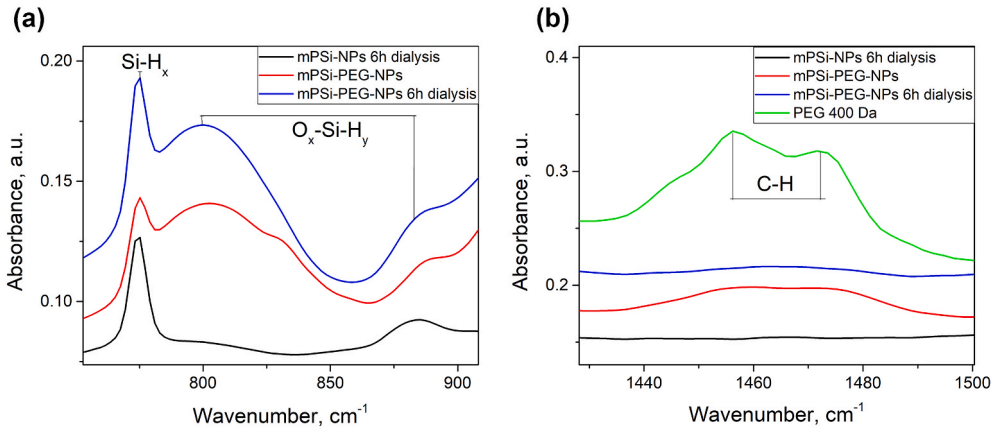

Fig. 8. FTIR absorption spectra of mPSi-NPs after 6 h dialysis (black curve), mPSi-PEG-NPs (red curve), mPSi-PEG-NPs after 6 h dialysis (blue curve), and PEG 400 Da (green curve): (a) region of the C-H bonds in PEG, (b) region of the Si–H_x and O_xSi-H_y bonds in mPSi. (For interpretation of the references to colour in this figure legend, the reader is referred to the Web version of this article.)

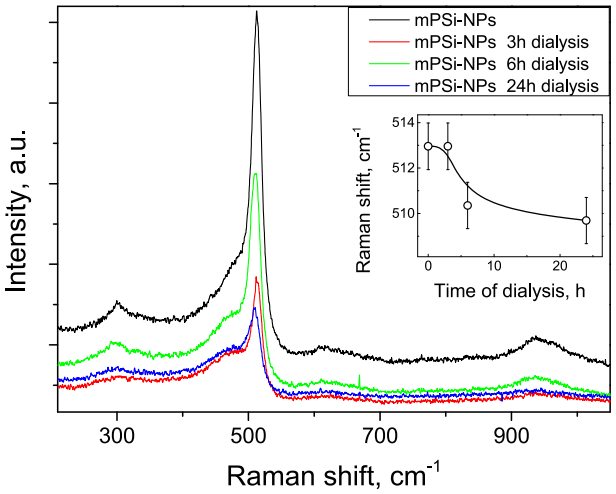

Fig. 9. Raman spectra of mPSi-NPs (black curve), mPSi-NPs after 3 h dialysis (red curve), mPSi-NPs after 6 h dialysis (green curve) and mPSi-NPs after 24 h dialysis (blue curve). Insert shows dependence of the Raman peak position during dialysis time. ND filter 1 dB, acc. time 60s. (For interpretation of the references to colour in this figure legend, the reader is referred to the Web version of this article.)

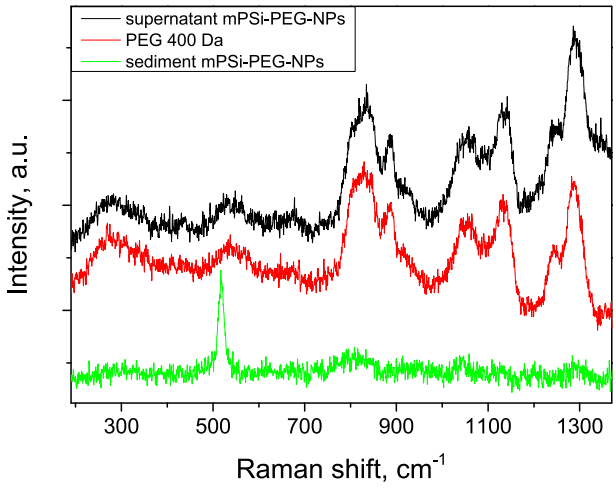

Fig. 10. Raman spectra of supernatant mPSi-PEG-NPs (black curve), PEG 400 Da (red curve), and sediment mPSi-PEG-NPs (green curve). ND filter 0.4 dB, acc. time 60s. (For interpretation of the references to colour in this figure legend, the reader is referred to the Web version of this article.)

concept of the electrochemical formation of porous silicon, the Si-H_x bonds form during etching in aqueous hydrofluoric acid solution [24]. A lot of research is devoted to learning about the possibility of using porous silicon as hydrogen reservoirs [26,27]. However, during storage of porous silicon in air or in aqueous media the Si-H_x groups are replaced by the O_x-Si-H_y and Si-O_x groups and dehydrogenation of the surface takes place [24,25]. Thus, the FTIR data demonstrate a mixed oxide-hydride composition of the pore surface coating in mPSi-NPs that ensures their hydrophilic properties and effective loading with drugs, including those with a low degree of solubility in water.

Red curve in Fig. 7 shows the FTIR spectrum of mPSi-PEG-NPs, which reveals both the mPSi-related bonds and PEG vibration modes. The latter modes result in the intense narrow bands at 1250, 1300, 1456 and 2930 cm^{-1} assigned to the C–H stretching vibrations [18].

The PEG content in mPSi-PEG-NPs was determined from the intensity of the peak at 1456 cm^{-1} (see Fig. 8a). About 50% of PEG was bound to mPSi-NPs during grinding and centrifugation. The dialysis for 6 h reduces the PEG content by 30%. We also observe the retention of Si–H_x and O_x-Si-H_y bonds after the interaction of mPSi-NPs with PEG (see Fig. 8b), which indicates the protective effect of PEG. The intensity of the peaks of Si–O bonds in the mPSi-PEG-NPs increases. It can be assumed that the PEG coating of NPs prevents the dissolution of the latter, while the silicon oxide layer becomes more developed.

Thus, according to the FTIR absorption spectra, we can say that PEG is a preservative for mPSi-NPs not only at the initial stage, but also remains on the surface after a while.

3.6. Raman spectroscopy

A Horiba Jobin Yvon LabRAM HR Visible micro-Raman spectrometer was used to measure Raman spectra of dried mPSi-NPs and mPSi-PEG-NPs. Fig. 9 shows Raman spectra of mPSi-NPs before and after storage in water in dialysis mode. The Raman intensities of these samples were very low relative to the signal from undoped c-Si wafers, so a lens with 50× magnification was used for better detection. This can be explained by amorphization of some Si nanocrystals in the process of their preparation by mechanical grinding of porous layers. The Raman spectrum contains broadband with a maximum at 480–490 cm^{-1}, which is usually associated with the amorphous silicon phase [28].

The peak corresponding to the Raman scattering by optical phonons of the c-Si lattice (520.5 cm^{-1}) in mPSi-NPs spectrum is shifted to 513 cm^{-1} due to the heating of the samples. Moreover, the peak gradually

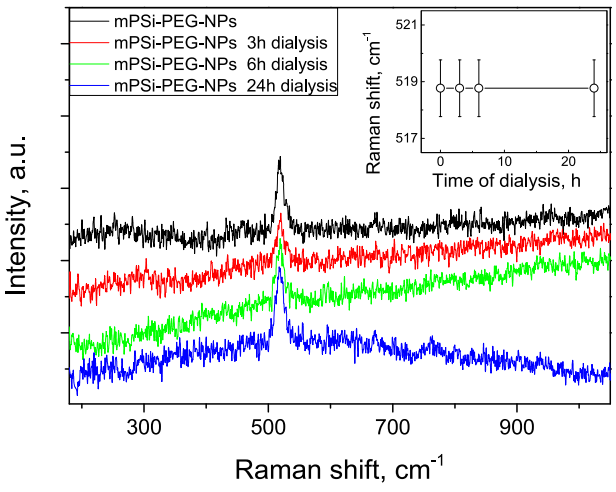

Fig. 11. Raman spectra of mPSi-PEG-NPs (black curve), mPSi-PEG-NPs after 3 h dialysis (red curve), mPSi-PEG-NPs after 6 h dialysis (green curve), and mPSi-PEG-NPs after 24 h dialysis (blue curve). Insert - displacement of the Raman peak of silicon during dialysis. ND filter 0.4 dB, acc. time 60s. (For interpretation of the references to colour in this figure legend, the reader is referred to the Web version of this article.)

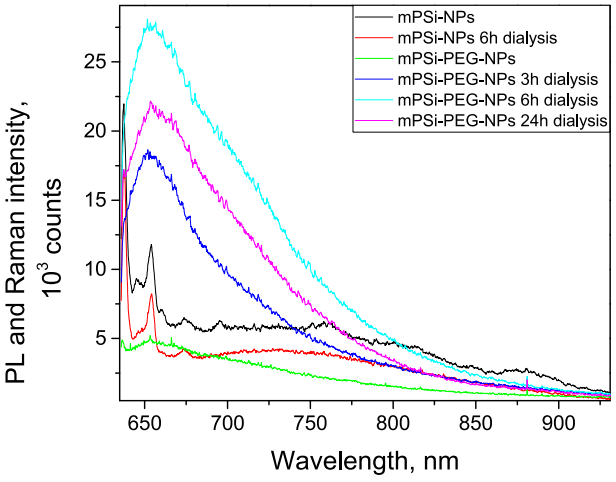

Fig. 12. Raman and PL spectra of mPSi-NPs (black curve), mPSi-NPs after 6 h dialysis (red curve), mPSi-PEG-NPs (green curve), mPSi-PEG-NPs after 3 h dialysis (blue curve), mPSi-PEG-NPs after 6 h dialysis (cyan curve), and mPSi-PEG-NPs after 24 h dialysis (pink curve). Excitation wavelength 633 nm. (For interpretation of the references to colour in this figure legend, the reader is referred to the Web version of this article.)

shifts to the left with increasing dialysis time, i.e. the dissolution is accompanied by a decrease of size. This manifestation of the size effect is shown in the inset in Fig. 10 where the Raman shift decreases with time of the dialysis. There is also an increase in the relative contribution of the amorphous phase in mPSi-NPs (shoulder at 480-490 cm^{-1}) during dialysis, and it can be explained by the fact that for nanocrystals with small sizes, the degree of disordering of the crystal lattice increases because of interaction with water and oxygen molecules [29]. The large width of the peak indicates the presence of silicon nanocrystals with a wide size distribution, that is in good agreement with the SEM data (see Fig. 3). Also, when the samples are kept in water, there is a significant decrease in the intensity of the Raman spectrum, that is explained by the dissolution of some of the nanocrystals.

After grinding mPSi in PEG, the centrifugation at high speed (30 min, 15000 rpm, 21000 rcf) was performed to separate mPSi-PEG-NPs from unbound PEG molecules. As one can see from Fig. 8 the supernatant's spectrum coincides with that of PEG, in which the grinding was carried out, and the spectrum of mPSi-PEG-NPs sediment consists of the PEG-related peaks of low intensity.

Fig. 11 shows spectra of the Raman scattering of mPSi-PEG-NPs before and after dialysis in water for the time up to 24 h. As one can see from the comparison of Figs. 10 and 11 the intensity of PEG associated peaks is very low for mPSi-PEG-NPs, while the Raman peak of c-Si lattice at 520.5 cm^{-1} is well detectible for these NPs. Moreover, the Raman peak position does not change with the time of dialysis (see inset in Fig. 11). Therefore, mPSi-NPs with PEG coating retain both the crystalline lattice and the mean size of Si nanocrystals that is in contrast with uncoated mPSi-NPs (compare Figs. 9 and 11). The larger noise in the Raman spectra of mPSi-PEG-NPs (see Fig. 11) in comparison with that for mPSi-NPs (see Fig. 9) can be related to the photoluminescence (PL) of the former NPs.

Fig. 12 shows spectra of both the Raman scattering and PL of mPSi-NPs and mPSi-PEG-NPs just after preparation and after dialysis in water. The stronger PL of mPSi-PEG-NPs indicates that PEG stabilizes the inner surface of mPSi-NPs, which leads to the passivation of non-radiative recombination centers on the surface. Because mPSi-PEG-NPs don't show significant changes in the Raman signal after exposure to water, the passivation is obviously related to the higher stability of PEGylated NPs to dissolution in water.

4. Conclusions

Nanoparticles of porous silicon are covered with PEG-400 molecules by using a simple and convenient method of the mechanical grinding of porous silicon films in aqueous medium. The method allows us to perform the PEGylation simultaneously with the nanoparticle formation and to stabilize the nanoparticles against dissolution in water. The ability to inhibit the dissolution of mesoporous silicon nanoparticles by PEGylation has been confirmed by means of the dynamic light scattering, energy dispersive spectroscopy, Fourier transform infrared spectroscopy, photoluminescence and Raman spectroscopy. The prepared nanoparticles have porous morphology that can be used to accommodate various payloads. Furthermore, because of the demonstrated luminescence property, PEG-grafted mesoporous silicon nanoparticles can be also used as luminescent labels in biomedicine.

CRediT authorship contribution statement

A.S. Eremina: Writing – original draft, Visualization, Investigation. **Yu V. Kargina:** Investigation, Writing – review & editing. **A. Yu Kharin:** Writing – review & editing, Investigation. **D.I. Petukhov:** Investigation. **V. Yu Timoshenko:** Conceptualization, Data curation, Validation, Writing – review & editing, Writing – review & editing, Validation, Data curation, Conceptualization.

Declaration of competing interest

The authors declare that they have no known competing financial interests or personal relationships that could have appeared to influence the work reported in this paper.

Acknowledgments

The authors acknowledge the support by the Grant from the Ministry of Science and Higher Education of the Russian Federation (FSWU-2020-0035) and A.Yu.K. thanks the support of his work by the Grant of the President of the Russian Federation (MK-5375.2021.1.3).

Appendix A. Supplementary data

Supplementary data to this article can be found online at https://doi.org/10.1016/j.micromeso.2021.111641.

References

[1] L. Canham, Handbook of Porous Silicon, second ed., Springer, New York, 2018 https://doi.org/10.1007/978-3-319-71381-6.

[2] E.J. Anglin, et al., Porous silicon in drug delivery devices and materials, Adv. Drug Deliv. Rev. 60 (11) (2008) 1266–1277, https://doi.org/10.1016/j.addr.2008.03.017.

[3] J. Park, et al., Biodegradable luminescent porous silicon nanoparticles for in vivo applications, Nat. Mater. 8 (2009) 331–336, https://doi.org/10.1038/nmat2398.

[4] M.A. Konoplyannikov, et al., Mesoporous silicon nanoparticles loaded with salinomycin for cancer therapy applications, Microporous Mesoporous Mater. (2021) (to be published).

[5] L.A. Osminkina, V.Yu Timoshenko, Porous silicon as a sensitizer for biomedical applications, Mesoporous Biomater. 3 (2016) 39–48, https://doi.org/10.1515/mesbi-2016-0005.

[6] A.F. Alykova, et al., Raman diagnostics of silicon nanocrystals dissolution in aqueous medium, J. Phys. (Paris): Conf. Series 945 (2018), 012002, https://doi.org/10.1088/1742-6596/945/1/012002.

[7] A.Yu Kharin, Y.V. Kargina, V.Yu Timoshenko, Evolution of nanocrystal size distribution in porous silicon nanoparticles during storage in aqueous media: X-ray diffraction analysis, J. Nanoparticle Res. 21 (27) (2019) 1–7, https://doi.org/10.1007/s11051-019-4466-9.

[8] K. Sato, et al., Characterization of orientation-dependent etching properties of single-crystal silicon: effects of KOH concentration, Sensors Actuators A Phys 64 (1) (1998) 87–93, https://doi.org/10.1016/S0924-4247(97)01658-0.

[9] L.T. Canham, Nanoscale semiconducting silicon as a nutritional food additive, Nanotechnology 18 (18) (2007), 185704, https://doi.org/10.1088/0957-4484/18/18/185704.

[10] V.A. Oleshchenko, et al., Localized infrared radiation-induced hyperthermia sensitized by laser-ablated silicon nanoparticles for phototherapy applications, Appl. Surf. Sci. 516 (2020), 145661, https://doi.org/10.1016/j.apsusc.2020.145661.

[11] A.P. Sviridov, et al., Cytotoxicity control of silicon nanoparticles by biopolymer coating and ultrasound irradiation for cancer theranostic applications, Nanotechnology 28 (10) (2017), 105102, https://doi.org/10.1088/1361-6528/aa5b7c.

[12] YuA. Polkovnikova, et al., Porous silicon nanoparticles containing neurotropic drugs, Inorg. Mater. 53 (2017) 477–483, https://doi.org/10.1134/S0020168517050156.

[13] F. Zhang, et al., Polymer-coated nanoparticles: a universal tool for biolabelling experiments, Small 7 (22) (2011) 3113–3127, https://doi.org/10.1002/smll.201100608.

[14] L.A. Osminkina, et al., Porous silicon nanoparticles as efficient sensitizers for sonodynamic therapy of cancer, Microporous Mesoporous Mater. 210 (2015) 169–175, https://doi.org/10.1016/j.micromeso.2015.02.037.

[15] I. Rio-Echevarria, et al., Highly PEGylated silica nanoparticles: “ready to use” stealth functional nanocarriers, J. Mater. Chem. 20 (2010) 2780–2787, https://doi.org/10.1039/B921735E.

[16] M.J. Roberts, M.D. Bentley, J.M. Harris, Chemistry for peptide and protein PEGylation, Adv. Drug Deliv. Rev. 54 (2002) 459–476, https://doi.org/10.1016/s0169-409x(02)00022-4.

[17] D. Gallacha, et al., Functionality of porous silicon particles: surface modification for biomedical applications, Mater. Sci. Eng., B 169 (2010) 123–127, https://doi.org/10.1016/j.mseb.2009.12.001.

[18] S.P. Low, et al., Evaluation of mammalian cell adhesion on surface-modified porous silicon, Biomaterials 27 (26) (2006) 4538–4546, https://doi.org/10.1016/j.biomaterials.2006.04.015.

[19] B.C. Kieseier, P.A. Calabresi, PEGylation of interferon-β-1a, CNS Drugs 26 (2012) 205–214, https://doi.org/10.2165/11596970-000000000-00000.

[20] A.V. Kuchumova, et al., Modification of recombinant asparaginase from erwinia carotovora with polyethylene glycol 5000, Biochemistry (Moscow) Supplement Series B: Biomed. Chem. 1 (2007) 230–232, https://doi.org/10.1134/S1990750807030092.

[21] A.Yu Kharin, Deep learning for scanning electron microscopy: synthetic data for the nanoparticles detection, Ultramicroscopy 219 (2020), 113125, https://doi.org/10.1016/j.ultramic.2020.113125.

[22] R. Herino, et al., Porosity and pore size distribution of porous silicon layers, J. Electrochem. Soc. 134 (1987) 1994–2000, https://doi.org/10.1149/1.2100805.

[23] L.A. Osminkina, et al., J. Nanoparticle Res. 16 (2014) 2430, https://doi.org/10.1007/s11051-014-2430-2.

[24] Y. Ogata, et al., Oxidation of porous silicon under water vapor, J. Electrochem. Soc. 142 (5) (1995) 1595–1601, https://doi.org/10.1149/1.2048619.

[25] P. Gupta, et al., FTIR studies of H2O and D2O decomposition on porous silicon surfaces, Surf. Sci. 245 (1991) 360–372, https://doi.org/10.1016/0039-6028(91)90038-T.

[26] A.I. Manilov, V.A. Skryshevsky, Hydrogen in porous silicon—a review, Mater. Sci. Eng., B 178 (15) (2013) 942–955, https://doi.org/10.1016/j.mseb.2013.05.001.

[27] V. Lysenko, et al., Study of porous silicon nanostructures as hydrogen reservoirs, J. Phys. Chem. B 109 (42) (2005) 19711–19718, https://doi.org/10.1021/jp053007h.

[28] S.V. Gaisler, et al., Analysis of Raman spectra of amorphous-nanocrystalline silicon films, Phys. Solid State 46 (2004) 1528–1532, https://doi.org/10.1134/1.1788789.

[29] E. Tolstik, et al., Studies of silicon nanoparticles uptake and biodegradation in cancer cells by Raman spectroscopy, Nanomed. Nanotechnol. Biol. Med. 12 (7) (2016) 1931–1940, https://doi.org/10.1016/j.nano.2016.04.004.